1 **Revision 3**

2 **Hydrous wadsleyite crystal structure up to 32 GPa**

3 Word count: 8621

4 Fei Wang[a,b], Elizabeth C. Thompson[c], Dongzhou Zhang[d], Jingui Xu[d], Ercan E. Alp[e], Steven D. Jacobsen[a]

5

6 [a] *Department of Earth and Planetary Sciences, Northwestern University, Evanston, IL 60208, USA*

7 [b] *Bayerisches Geoinstitut, University of Bayreuth, Bayreuth, Germany*

8 [c] *Department of Earth and Environmental Systems, The University of the South, Sewanee, TN 37383, USA*

9 [d] *Hawai'i Institute of Geophysics and Planetology, School of Ocean and Earth Science and Technology,*

10 *University of Hawai'i at Manoa, Honolulu, HI 96822*

11 [e]*Advanced Photon Source, Argonne National Laboratory, Argonne, IL 60439 USA*

12

13 Corresponding author: Fei Wang (feiwang2020@u.northwestern.edu)
14

15 **Abstract**

16 Hydroxylation of wadsleyite, β-$(Mg,Fe)_2SiO_4$, is associated with divalent cation defects and well

17 known to affect its physical properties. However, an atomic-scale understanding of the defect structure

18 and hydrogen bonding at high pressures is needed to interpret the influence of water on the behavior of

19 wadsleyite in the mantle transition zone. We have determined the pressure evolution of the wadsleyite

20 crystal symmetry and structure, including all O…O interatomic distances, up to 32 GPa using single-

21 crystal X-ray diffraction on two well-characterized, Fe-bearing (Fo_{90}) samples containing 0.25(4) and

22 2.0(2) wt% H_2O. Both compositions undergo a pressure-dependent monoclinic distortion from

23 orthorhombic symmetry above 9 GPa, with the less hydrous sample showing a larger increase in

24 distortion at increased pressures due to the difference in compressibility of the split M3 site in the

25 monoclinic setting arising from preferred vacancy ordering at the M3B site. Although hydrogen positions

26 cannot be modeled from the X-ray diffraction data, the pressure evolution of the longer O1…O4 distance

27 in the structure characterizes the primary hydrogen bond length. We observe the hydrogen-bonded

28 O1…O4 distance shorten gradually from 3.080(1) Å at ambient pressure to about 2.90(1) Å at 25 GPa,

29 being still much longer than is defined as strong hydrogen bonding (2.5–2.7 Å). Above 25 GPa and up to

30 the maximum pressure of the experiment at 32.5 GPa, the hydrogen-bonded O1…O4 distance decreases

31 no further, despite the fact that previous spectroscopic studies have shown that the primary O–H

32 stretching frequencies continuously drop into the regime of strong hydrogen bonding (<3200 cm^{-1}) above

33 ~15 GPa. We propose that the primary O1–H…O4 hydrogen bond in wadsleyite becomes highly non-

34 linear at high pressures based on its deviation from frequency-distance correlations for linear hydrogen

35 bonds. One possible explanation is that the hydrogen position shifts from being nearly on the long O1–O4

36 edge of the M3 site to a position more above O1 along the c-axis.

37

38 Keywords: Wadsleyite, mantle transition zone, hydrogen bond, water

39

40   **Introduction**

41   The nominally anhydrous minerals (NAMs) wadsleyite and ringwoodite can incorporate 1–2 wt%

42 H_2O into their crystal structures as hydroxyl groups at the elevated pressures and temperatures of the

43 Earth's mantle transition zone (e.g., Smyth 1987; Fei and Katsura 2020), which suggests that the Earth's

44 mantle could play a dynamic role in the evolution of surface water reservoirs over geologic time (Dong et

45 al. 2021). Although no samples of terrestrial wadsleyite have been reported, the recent discovery of

46 hydrous ringwoodite containing ~1.5 wt% water, found as a natural inclusion in a diamond (Pearson et al.

47 2014), provides evidence that the transition zone is locally hydrated. Mapping regional-scale hydration

48 from seismological data (e.g., Karato 2011; Wang et al. 2018) requires knowledge of the effects of

49 hydration on the physical properties of NAMs at transition zone pressures and temperatures. For example,

50 theory and experiments show that the incorporation of even small quantities of H_2O significantly

51 influence the elastic properties of wadsleyite governing the velocity of seismic waves (e.g., Tsuchiya and

52   Tsuchiya 2009; Mao et al. 2011; Buchen et al. 2018; Gwanmesia et al. 2020). As the elastic properties of

53   Earth materials are ultimately controlled by interatomic potentials, knowledge of the crystal structure and

54   evolution of hydrogen bonding in wadsleyite is useful in predicting the physical properties expected for

55   hydrous and anhydrous regions of the upper transition zone.

56   The crystal structure of wadsleyite is unique among the Mg_2SiO_4 polymorphs in possessing a

57   sorosilicate group (Si_2O_7). The structure consists of three octahedral metal cation sites (M) occupied by

58   Mg^{2+}, Fe^{2+} or Fe^{3+}, one tetrahedral site (T) occupied by Si^{4+} or Fe^{3+}, and four distinct oxygen sites

59   (Horiuchi & Sawamoto 1981, Smyth et al. 1997) (Figure S1). The first step in understanding the impacts

60   of hydration on the physical and mechanical properties of wadsleyite and other NAMs is determining

61   where hydrogen is structurally accommodated and charge-balanced by associated cation defect vacancies.

62   Smyth et al. (1987) recognized that the O1 site of wadsleyite is a favorable location for H based on the

63   electrostatic potential as this site is coordinated to five Mg sites but no Si, and is therefore under-bonded.

64   Shortly thereafter, McMillan et al. (1991) observed OH absorption bands in wadsleyite using Fourier

65   transform infrared (FTIR) spectroscopy on wadsleyite crystals that had been fortuitously hydrated during

66   synthesis by dehydration of the pyrophyllite pressure medium.

67   The pleochroic behavior of OH absorbance observed in polarized FTIR spectra (Jacobsen et al.

68   2005) showed that the primary OH bands at 3300–3400 cm^{-1} can be explained by H at the O1 site, with

69   protonation of the unshared O1–O4 edge of the M3 site, where most cation vacancies were observed.

70   Jacobsen et al. (2005) also noted that some protonation may occur along the shorter O1–O4 edge of the

71   M3 site that is shared with the M2 site, as well as possibly along the O1–O3 edge of the M3 site. Similar

72   sites were proposed from room-pressure XRD and high-pressure FTIR spectroscopy measurements by

73   Dion et al. (2010). Sano-Furukawa et al. (2011) refined the H positions in wadsleyite using powder

74   neutron diffraction data and confirmed that the dominant hydrogen site is located close to O1 and along

75   the longer of the two distinct O1–O4 edges of the M3 site, with minor occupation along the O1–O3 edge

76   of the M3 site. Using single-crystal neutron diffraction data, Purevjav et al. (2016) confirmed that the

77   major H site is along the longer and unshared O1–O4 edges of the M3 site with an O–H distance of ~1 Å

3

78   and slightly non-linear hydrogen bond angle of 171°. Whereas the longer O1–O4 edges of M3 site appear

79   to host the majority of H in wadsleyite, realistically there are also many minor sites, as evidenced by up to

80   15 observed O–H stretching frequencies, which can tentatively be assigned to other sites in the structure

81   based on frequency-distance correlations (Libowitzky, 1999; Kohn et al. 2002).

82   In silicates and oxides, hydrogen bonds form when a hydrogen atom, bonded to a donor oxygen

83   atom via a polar covalent bond, interacts electrostatically with a nearby acceptor oxygen (Emsley 1981).

84   Hydrogen bonds have both a characteristic bond length, $d(O…O)$, defined by the distance between the

85   donor and acceptor oxygen atoms along O–H…O, and a characteristic O–H stretching frequency, which

86   is corelated to hydrogen-bond strength, assuming the hydrogen bond angle along O–H…O is close to 180°

87   (Libowitzky, 1999). Typically, hydrogen bonds form an asymmetric potential well between donor and

88   acceptor oxygen atoms, where the O–H bond is shorter than the H…O distance. Although hydrogen

89   bonds in minerals have a poorly defined upper limit beyond ~3 Å, strong hydrogen bonds are defined as

90   having $d(O…O)$ of 2.5–2.7 Å (Libowitzky, 1999). On compression, if $d(O…O)$ shortens, the O–H bond

91   lengthens due to the increased attractive force of the acceptor oxygen, weakening the O–H bond and

92   lowering the O–H stretching frequency (Libowitzky 1999). Whereas the O–H stretching frequencies in

93   most hydrous minerals are observed at 3200–4000 cm^{-1}, strong hydrogen bonds have stretching

94   frequencies in the range of 1600–3200 cm^{-1}.

95   High-pressure FTIR spectroscopy studies of wadsleyite have shown that the primary O–H

96   stretching bands associated with hydrogen bonding along the O1–O4 edge at 3300–3400 cm^{-1} shift

97   strongly with increasing pressure to lower frequencies of about 3150–3250 cm^{-1} at 16–18 GPa, the

98   maximum pressure of those experiments (Deon et al. 2010; Yang et al. 2014). This is consistent with

99   earlier findings of Kleppe et al. (2006), who reported Raman spectroscopy measurements of hydrous Fe-

100 bearing wadsleyite up to approximately 50 GPa and found that the 3300-3400 cm^{-1} band became a very

101 broad and weak feature at frequencies below 3000 cm^{-1} above approximately 40 GPa. Because O–H

102 stretching frequencies in hydrous wadsleyite drop below ~3200 cm^{-1} above 15 GPa, they enter the regime

103 of strong hydrogen bonding as defined for linear hydrogen bonds (Libowitzky 1999). Since the primary

4

104 hydrogen bond in wadsleyite, O1–H…O4, is rather long at room pressure with d(O1…O4) = 3.1 Å

105 (Jacobsen et al. 2005), a decrease of O–H stretching frequencies to below 3200 cm^{-1} above 15 GPa would

106 imply a drastic compression of the O1–O4 edge if the hydrogen bond remains fairly linear. One objective

107 of this study is to determine all the interatomic O…O distances in the wadsleyite structure up to 32 GPa

108 in part to test whether or not spectroscopic indications of O–H stretching frequencies below ~3200 cm^{-1}

109 are consistent with conventionally defined strong hydrogen bonds with d(O…O) <2.7 Å.

110 Another consequence of the hydration of wadsleyite is a change in symmetry from orthorhombic

111 (*Imma*) to monoclinic (*I2/m*), which is defined by the deviation of the unit-cell β-angle from 90.0°. This

112 was first recognized by Smyth et al. (1997) and subsequently observed, to varying degrees, by other

113 studies (e.g., Jacobsen et al. 2005; Holl et al. 2008). The breaking of orthorhombic symmetry in hydrous

114 wadsleyite is believed to result from the unequal distribution of vacancies at M3 sites, resulting in two

115 non-equivalent M3A and M3B sites (Smyth et al. 1997). A Raman spectroscopy study of Fe-bearing

116 wadsleyite with 2.4 wt% water by Kleppe et al. (2006) inferred monoclinic symmetry at high pressure and

117 suggested, based on Raman spectra, that the monoclinic angle might increase with pressure. In contrast,

118 Holl et al. (2008) evaluated the β-angle in wadsleyite containing 1.66 wt% H_2O up to 10 GPa but did not

119 observe a pressure-induced change in β-angle. Determining the structure and symmetry of hydrous

120 wadsleyite at pressures exceeding 10 GPa is necessary to more adequately understand the physical

121 properties of hydrous wadsleyite in the transition zone.

122 To date, only one experimental study (Hazen et al. 2000) has examined the structure of

123 wadsleyite at high pressures (P_{max} = 10.1 GPa) from single-crystal X-ray diffraction data, but the water

124 content of the samples in that study was not determined. Therefore, we have undertaken high-precision

125 structure refinements of well-characterized hydrous wadsleyite single crystals under quasi-hydrostatic

126 compression up to 35 GPa. To directly compare the effects of water, one sample contains ~2.0 wt% H_2O

127 while the other sample contains ~0.25 wt% H_2O. Both samples approximate the Fe-content of mantle

128 olivine (Fo$_{90}$). Our two main objectives are: (1) evaluate the crystal symmetry evolution with pressure,

129 and (2) determine the pressure-dependence of all interatomic O…O distances in the structure to compare

5

130   hydrogen-bonded versus non-hydrogen bonded O–O edges for comparison to previously observed O–H

131   stretching frequencies at high pressures. The results of this study help to explain the modified physical

132   properties of hydrous wadsleyite in the transition zone.

133

Materials and Methods

Sample synthesis and characterization

136   This study examines two different hydrous Fe-bearing wadsleyite samples from synthesis run

137   Z0570 containing 2.0(2) wt% H_2O and from run Z0902 containing 0.25(4) wt% H_2O (Chang et al. 2015).

138   Both samples were synthesized using the 5000-ton, multi-anvil press at Bayerisches Geoinstitut,

139   University of Bayreuth, Germany. For run Z0570, starting materials of San Carlos olivine plus liquid

140   water were welded into a Pt capsule, compressed to 18 GPa and heated to a peak temperature of 1400 °C

141   for several minutes before annealing at 1100 °C for 30 minutes. Run products from Z0570 consisted of

142   both wadsleyite and ringwoodite. For run Z0902, San Carlos olivine was used without the addition of

143   water and compressed to 11 GPa for annealing at 1100 °C (Chang et al. 2015). No phase other than

144   wadsleyite was observed in the run product of Z0902. Electron microprobe analyses give values of

145   Mg/(Mg+ΣFe) of 0.89 and 0.90 for run Z0570 and run Z0902, respectively (Chang et al. 2015). FTIR

146   spectra for both samples are presented in Chang et al. (2015) and indicate 1.4 wt% H_2O and 0.25 wt%

147   H_2O in run Z0570 and Z0902, respectively, using the calibration of Deon et al. (2010). The water content

148   of Z0570 was also measured at two secondary ion mass spectrometry laboratories by Chang et al. (2015),

149   resulting in 1.93(22) wt% H_2O and 2.07(24) wt% H_2O. Since FTIR methods are less reliable for very high

150   water contents in wadsleyite, we used 2.0(2) wt% H_2O for the more hydrous sample (Z0570) and 0.25(4)

151   wt% H_2O for the less hydrous sample (Z0902).

152

Synchrotron Mössbauer Spectroscopy

6

154   To determine the oxidation states of iron, time-domain synchrotron Mössbauer spectroscopy

155   (SMS) was conducted on beamline 3-ID-B of the Advanced Photon Source (APS), Argonne National

156   Laboratory. One ~150 μm diameter grain was selected from each synthesis run. A Si (111) double crystal

157   monochromator and a 4-bounce inline high-resolution monochromator (Toellner 2000) was used to filter

158   the X-ray energy to a bandwidth of 1 meV at 14.4125 keV. The monochromatic X-rays were focused into

159   a 15 μm diameter beam using a Kirkpatrick-Baez type mirror. The nuclear delay signal was recorded in

160   the 21–128 ns time window between the X-ray pulses generated by the synchrotron. Time-domain

161   Mössbauer spectra were fit using CONUSS 2.2.0 (Sturhahn, 2000) to get the hyperfine parameters of Fe

162   and the ferric-to-ferrous ratio for each sample. A two-doublet model was used to fit each spectrum, with

163   one doublet each for Fe^{2+} and Fe^{3+}, as it gave the best statistical fit. The isomer shift of Fe^{2+} was fixed at

164   1.04 mm/s relative to stainless steel based on previous Mössbauer data (Chang et al. 2015).

165

166   **Sample loading environment and pressure determination**

167   High pressures were achieved by loading samples into one of two short symmetric type diamond

168   anvil cells (DACs) with either a 78° or 81° opening angle. Sample chambers of 180 μm diameter were

169   laser ablated into rhenium gaskets that were pre-indented to ~40 μm thickness. For each sample, a single

170   crystal of wadsleyite ~30 μm in diameter was parallel-polished down to a thickness of ~10 ± 2 μm. Each

171   sample was loaded into a DAC equipped with Boehler-Almax diamond anvils with 300 μm culets. Two

172   ruby spheres were placed inside each cell as pressure standards, with one ruby placed close to the center

173   of the sample chamber to serve as the primary pressure standard and the other ruby placed near the edge

174   of the sample chamber to monitor the possible development of pressure gradients. Ruby pressures were

175   calculated from the shift of the R_1 ruby fluorescence line using the quasi-hydrostatic calibration from

176   Jacobsen et al. (2008). Neon was loaded using the COMPRES-GSECARS gas loading system (Rivers et

177   al. 2008) to serve as a quasi-hydrostatic pressure-transmitting medium.

178

179   **X-ray diffraction experiments**

180　　　　　Single-crystal X-ray diffraction (XRD) data were collected on beamline 13-BM-C of the APS.

181　　The incident X-ray beam was monochromatized with a silicon (311) crystal to 0.434 Å incident

182　　wavelength with 1 eV energy bandwidth and focused to a 15×15 μm^2 spot. A Pilatus 1M (Dectris)

183　　detector with 1 mm thick silicon sensor was used to record the diffraction patterns. The sample-to-

184　　detector distance and the tilt of the detector was calibrated using LaB$_6$ (Zhang et al. 2017). At each

185　　pressure, step scans were collected in steps of 1° at 1s/deg in the φ direction using a detector with two

186　　collecting positions. The collecting positions were moved to be positioned 20° apart in 2θ angle.

187　　Diffraction intensity data for crystal structure refinements were collected at ambient conditions before gas

188　　loading and at each subsequent pressure step. High-pressure data were collected by compressing the DAC

189　　with a gas membrane cell at pressure intervals of 1–1.5 GPa. After increasing the pressure at each

190　　pressure step, the sample was allowed to sit for 10–15 min before data collection to stabilize the pressure.

191　　The reported pressures are the average of pressures measured before and after XRD data collection. The

192　　reported uncertainty is half of the absolute pressure difference before and after XRD collection. When this

193　　pressure difference was smaller than 0.1 GPa, 0.1 GPa was used as the pressure uncertainty to reflect the

194　　linewidth of the ruby fluorescence spectrum.

195　　　　　Diffraction intensities and unit cell parameters were obtained using the APEX3 software (Bruker).

196　　SHELXL (Dolomanov et al. 2009; Sheldrick 2015) with the Olex2 general user interface was used to

197　　refine the crystal structure using peak intensities reduced by the APEX3 software. All crystal structures

198　　were refined using intensity data collected from both of the collecting positions of the detector. Two

199　　models were used to refine the crystal structure: an orthorhombic (*Imma*) model from Jacobsen et al.

200　　(2005) and a monoclinic (*I2/m*) model from Smyth et al. (1997). The difference between them is that

201　　Smyth et al. (1997) splits the M3 site into two non-equivalent sites denoted M3A and M3B, and O4 site is

202　　split into O4A and O4B, where O4A is bonded to M3A and O4B bonded to M3B. Refinement parameters

203　　at each pressure step including the 2θ range, number of reflections, *hkl* range, and merging, and internal

204　　R-factors are listed in Tables S1 and S2.

205

206 <div align="center">**Results**</div>

207 **Mössbauer Spectroscopy**

208   Ambient-pressure SMS data for the more hydrous wadsleyite (Z0570) show that 24.7(1.1)% of

209 the total Fe was Fe^{3+} with an isomer shift of 0.082(9) mm/s and quadrupole splitting of 0.358(9) mm/s.

210 The quadrupole splitting for Fe^{2+} was 2.638(3) mm/s. For the less hydrous wadsleyite sample (Z0902),

211 12.8(1.0)% of the total Fe was Fe^{3+} with an isomer shift of 0.106(17) mm/s and quadrupole splitting of

212 0.25(2) mm/s. The quadrupole splitting for the Fe^{2+} site was 2.657(4) mm/s (Table 1). The isomer shifts

213 (relative to stainless steel) and quadrupole splitting values reported here for Z0570 are an improvement

214 over those measured by conventional Mössbauer spectroscopy in Chang et al. (2015) because of

215 improved signal-to-noise ratio in the current data. Chang et al. (2015) did not measure the Fe^{3+} content of

216 Z0902. Combining the current SMS results with the major element analyses and water content

217 determinations from Chang et al. (2015), we obtain the chemical formulas

218 $\left(Mg^{2+}_{1.638}Fe^{2+}_{0.145}Fe^{3+}_{0.047}\right)H_{0.320}SiO_4$ for sample Z0570 and $\left(Mg^{2+}_{1.782}Fe^{2+}_{0.173}Fe^{3+}_{0.025}\right)H_{0.041}SiO_4$ for sample

219 Z0902. The measured time-domain spectra and calculated energy-domain spectra of the best-fit hyperfine

220 model are shown in Figure S2.

221

222 **Equations of State**

223   Our ambient-pressure diffraction data show that sample Z0902 (0.25 wt% H_2O) has a slight

224 monoclinic distortion, with $\beta = 90.034(18)°$ and lattice parameters of $a_0 = 5.7119(5)$, $b_0 = 11.4785(5)$, $c_0 =$

225 8.282(2), resulting in a calculated unit cell volume of 543.00(14)$Å^3$. The more hydrous wadsleyite sample,

226 Z0570 (2 wt% H_2O), also has a slight monoclinic distortion, with $\beta = 90.015(3)°$ and lattice parameters of

227 $a_0 = 5.6965(2)$, $b_0 = 11.5431(4)$, $c_0 = 8.269(3)$, resulting in a calculated unit cell volume of 543.7(2) $Å^3$.

228 Based on these unit cell volumes and the detailed compositions given above, the reference density for the

229 more hydrous sample Z0570 is $\rho_0 = 3.5064(13)$ g/cm^3, and that for the less hydrous sample Z0902 is $\rho_0 =$

230 3.584(1) g/cm^3.

231   During compression up to about 10 GPa, the β-angle for both samples was essentially invariant.

232   However, above 9 GPa, both samples exhibit a linearly increasing β-angle with pressure, although by

233   markedly different amounts (Figure 1). Whereas the β-angle in the more hydrous sample (Z0570) only

234   increased by about 0.1° between 10 and 30 GPa, reaching 90.09(2)° at the highest pressure of 33 GPa, the

235   β-angle of the less hydrous sample (Z0902) increased by nearly 0.5°, reaching a value of 90.53(4)° at the

236   maximum pressure of 35 GPa. The lattice parameters at each pressure refined for both orthorhombic and

237   monoclinic symmetry for both samples are provided in Tables S3–S6.

238   Unit cell volumes were also calculated using both orthorhombic and monoclinic symmetry for

239   both samples at each pressure (Tables S3-S6). We fit the pressure–volume (P–V) data to a third-order

240   Birch-Murnaghan equation of state (BM3-EOS), where K_{T0} is the reference bulk modulus at ambient

241   pressure, K_{T0}' is the first pressure derivative of the bulk modulus evaluated at $P = 0$, and V_0 is the

242   reference volume at ambient pressure. The EOS fit was performed with EOSFit7c (Angel et al. 2014).

243   The inverse of the measurement uncertainties were used as weights for least-squares fits. The resulting

244   EOS parameters for the more hydrous sample (Z0570) using orthorhombic symmetry are: $V_0 = 543.19(23)$

245   Å^3, $K_{T0} = 164.0(2.7)$ GPa, and $K_{T0}' = 4.26(23)$. Assuming monoclinic symmetry for Z0902 we obtain $V_0 =$

246   543.09(22) Å^3, $K_{T0} = 172.3(2.3)$ GPa, and $K_{T0}' = 3.91(15)$. Based on statistical significance, our preferred

247   EOS fit to the more hydrous sample (Z0570) assumes orthorhombic symmetry and monoclinic symmetry

248   for the less hydrous sample (Z0902), which are plotted in Figure 2. EOS parameters for both

249   compositions in both crystal systems are given in Table S7.

250

251   **Structure Refinements**

252   Variation of the lattice parameters with pressure are plotted in Figure 3. A linearized third-order

253   BM-EOS fit was used to determine the linear compressibilities along the crystal axes (Angel et al. 2014).

254   The resulting linear moduli and axial compressibilities are given in Table S8. In both samples, the c-axis

255   is the most compressible, and the a- and b-axes have about the same compressibility. However, with

256   increased water content, the c-axis becomes more incompressible, while the a- and b-axes become more

257 compressible. We also evaluated the M–O bond lengths and polyhedral volumes as a function of pressure,

258 which are shown in Figures S3 and S4 and listed in Table S8. Compression data of all polyhedral volumes

259 are plotted in Figure 4.

260   The ambient-pressure structure refinements show vacancies only at the M3 sites, similar to what

261 has been observed in previous studies (Smyth et al. 1994; Jacobsen et al. 2005; Holl et al. 2008; Purevjav

262 et al. 2016). For the less hydrous and monoclinic sample (Z0902), the total site occupancies were 100%

263 for M1, M2, and M3A, but 94.9% in M3B, indicative of strongly preferred vacancy ordering onto the

264 M3B site, which has not previously been reported. The refined Fe occupancies at each site in Z0902 were

265 9.8% in M1, 3.8% in M2, 1.2% in M3A, and 9.4% in M3B. For the very hydrous sample (Z0570) we

266 observe no vacancy ordering between M3A and M3B and used the orthorhombic symmetry, finding the

267 total site occupancies were 100% for M1 and M2, but 87.8% in M3, consistent with there being more

268 hydrogen-related cation vacancies in the more hydrous sample. In Z0570, we refined Fe/Mg as well and

269 found 11.2% Fe in M1, 0.8% in M2, and 6.4% in M3.

270   The refined site occupancies obtained at room pressure were fixed for the high-pressure structure

271 refinements, except for the M3 site (M3A and M3B), which contains vacancies. However, we did not

272 observe significant changes in vacancy ordering with increasing pressure. Our results also suggest that

273 there is no Fe^{3+} at the T site of slightly hydrous wadsleyite, but up to 4% of the Fe cations may be at the T

274 site of very hydrous wadsleyite, consistent with previous findings (Smyth et al. 2014).

275   To illustrate how hydrogen potentially affects the compressibility of O–O octahedral edges in the

276 wadsleyite structure, we plot selected O–O distances as a function of pressure in Figure 5. A second-order

277 BM-EOS was used to fit the data with EOSFit7c (Angel et al. 2014). In Figure 5 we also plotted

278 prediction bands instead of confidence intervals to indicate that these are the error bars on quantities

279 calculated from a model, in contrast to error calculated directly from experimental data. The inverse of the

280 measurement uncertainties were used as weights in least-squares fits. The 95% prediction bands of the

281 O1–O4 (short) and O1–O1 edges for more hydrous and less hydrous wadsleyite nearly overlap, indicating

282 very similar compressibility. The long O1–O4 and O1–O3 edge, however, respond differently under

11

283 compression in the two samples: whereas the long O1–O4 edge is less compressible in the more hydrous

284 wadsleyite sample (Z0570), the O1–O3 edge is less compressible in the less hydrous wadsleyite. Most

285 notably, the longer O1–O4 edge in the more hydrous sample becomes incompressible above ~25 GPa

286 (Figure 5), but no comparable stiffening was observed in any other O–O distances, except possibly in the

287 O1–O3 edge of the more hydrous sample, which stiffens with a lesser degree of certainty. As stated

288 earlier, the longer O1–O4 octahedral edge is the primary hydrogen bond in wadsleyite (Sano-Furukawa et

289 al. 2011; Purevjav et al. 2016). A comprehensive overview of all O–O distances at the M1, M2, and M3

290 sites comparing both H_2O compositions is given in Figure S5.

291

292

293 **Discussion**

294 **Ordering in wadsleyite**

295 Our observation that Fe-bearing hydrous wadsleyite distorts from orthorhombic to monoclinic

296 symmetry with an increasing β-angle above 9 GPa could explain earlier observations of new Raman

297 peaks above ~9 GPa in the Raman spectra of hydrous Fe-bearing wadsleyite (Kleppe et al. 2006).

298 Jacobsen et al. (2005) and Holl et al. (2008) found that in pure-Mg wadsleyite there is a correlation

299 between monoclinic distortion and increasing water content. In contrast, in our Fe-bearing samples, our

300 less hydrous sample with 0.25 wt% H_2O actually deviates more from orthorhombic symmetry than the

301 more hydrous sample with ~2 wt% H_2O. To date, the crystal symmetry of hydrous wadsleyite has not

302 been investigated as a function of pressure. Surprisingly, on compression above 9 GPa, the less hydrous

303 sample deviates significantly more from orthorhombic symmetry than the more hydrous sample (Figure

304 1). Thus, the symmetry of Fe-bearing hydrous wadsleyite cannot be understood based on water content

305 alone.

306 In the less hydrous wadsleyite sample, the M3B octahedron has a slightly larger volume than the

307 M3A octahedron. This volume difference is related to M-site vacancies and may be caused by enhanced

308 O–O repulsion in the absence of a central cation (Jacobsen et al. 2005). If the larger polyhedral volume of

12

309   the M3B site is the result of a higher vacancy concentration as compared to the M3A site, the M3B site

310   can be expected to be more compressible, which is precisely what we observe in the polyhedral moduli

311   (Table 2) and interatomic distances (Table S9). Due to the increased compressibility of the M3B site, at

312   pressures exceeding 10 GPa it becomes smaller in volume than the M3A site (Table S12, S13, Figure S6),

313   which corresponds to the pressure at which we begin seeing the more distinct symmetry change from

314   orthorhombic to monoclinic. Orthorhombic symmetry in wadsleyite requires the plane perpendicular to

315   the b-axis between equivalent M3 sites as a mirror plane (Smyth et al. 1997; Ye et al. 2010, 2011). At low

316   pressure, this plane is almost perpendicular to the a-axis but slightly tilted. With increasing pressure, the

317   volume of the M3B octahedron decreases more than that of the M3A octahedron and at around 10 GPa

318   drops below the volume of the M3A octahedron (Table S12, S13, Figure S6), leading the (010) plane to

319   increasingly tilt, which breaks the mirror symmetry and causes the β-angle to deviate from 90°. In short,

320   the evolution of the $β$-angle at high pressures is likely due to the difference in vacancy population of the

321   two non-equivalent M3 sites and their corresponding differences in polyhedral compressibility. We

322   propose that the monoclinic distortion in wadsleyite increases with pressure when there is a significant

323   difference in the vacancy populations or in the Mg-Fe occupancies of the M3A and M3B sites, leading to

324   those sites having different compressibility and thus further distortion from orthorhombic symmetry. The

325   more hydrous wadsleyite sample in our study had no significant difference in the occupancies of the M3

326   sites, which have similar compressibility, thus the plane perpendicular to the b-axis was retained as a

327   mirror symmetry element

328   Our observations of changes in the crystal symmetry at ~9 GPa may shed light on some previous

329   spectroscopic observations. In Fe-free nominally anhydrous wadsleyite, Chopelas (1991) observed seven

330   Raman mode changes at 9.2 GPa, which the author posited as evidence of a second-order phase transition.

331   Cynn and Hofmeister (1994) reported high-pressure infrared data for Fe-bearing wadsleyite and described

332   a minor structure change at 9 GPa. Kleppe et al. (2006) reported the addition of four new Raman modes

333   in the mid-frequency range at 9 GPa in hydrous Fo_{90} wadsleyite. If the change in wadsleyite crystal

334   symmetry to monoclinic symmetry above 9 GPa is due to the M3 and O4 sites splitting into two non-

13

335   equivalent sites, the changes in vibrational modes are likely to result from a distortion of individual

336   octahedra since the affected vibrations are related to MgO6 octahedra. Our high-pressure structure data

337   could therefore potentially reconcile several previously observed changes in vibrational spectra at high

338   pressures.

339

340   **Influence of hydroxyl groups on the equation of state**

341   The elastic moduli and their pressure derivatives are needed to calculate density and sound

342   velocities at high pressures. For wadsleyite, previous studies have shown that the bulk modulus (K_0)

343   decreases with water content (e.g. Jacobsen 2005) and increases with iron content (e.g. Hazen 1993), as

344   recently reviewed by Buchen et al. (2017) and Wang et al. (2018). In agreement with these trends, our K_0

345   of ~164 GPa for hydrous Fo$_{89}$ wadsleyite with 2 wt% H_2O is about 6% lower than dry Fo$_{90}$ wadsleyite (Li

346   and Liebermann 2000; Liu et al. 2009). The relationship between water content and the pressure

347   derivative of the bulk modulus (K_0') shows no obvious trend (e.g., Chang et al. 2015). Holl et al. (2008)

348   suggested that K_0' should increase with water content because the strong O–O repulsive forces on

349   compression are ultimately a more important factor than the initially larger and more compressible

350   partially vacant M sites. But experiments by Holl et al. (2008) and Chang et al. (2015) found no link

351   between water content and K_0'. Unfortunately, attempts to resolve this discrepancy have been hampered

352   by a range of derived values for K_0' that can be dependent on experimental factors including data density,

353   pressure range, pressure medium, and pressure calibration, among others.

354   Buchen et al. (2018) obtained $K_{S0}' = 4.13(8)$ for a slightly hydrous wadsleyite (~0.24 wt.% water)

355   with Fo$_{89}$ composition using Brillouin spectroscopy, and $K_{T0}' = 4.4(2)$ on the same sample from static

356   compression using the BM3-EOS to $P_{max} = 20$ GPa with ruby pressures and 10 data points (Buchen et al.

357   2017), where the subscript S in K_{S0}' refers to the adiabatic bulk modulus and the subscript T in K_{T0}' refers

358   to the isothermal bulk modulus. Mao et al. (2011) and Chang et al. (2015) both evaluated the same

359   hydrous Fo$_{89}$ wadsleyite as this study (Z0570) with ~2 wt% water but Mao et al. (2011) reported $K_{S0}' =$

360   4.8(1) using Brillouin spectroscopy, while Chang et al. (2015) obtained $K_{T0}' = 3.77(14)$ from static

14

361   compression using a BM3-EOS to P_{max} = 32 GPa with ruby pressures and 31 data points. It should be

362   noted, however, that Chang et al. (2015) did not have an experimental V_0 value, which is an important

363   anchor in fitting K_{T0}' with the BM3-EOS because the derivative is effectively evaluated at zero pressure.

364   For comparison, we found K_{T0}' = 4.26(23) for Z0570 in this study using the BM3-EOS to P_{max} = 33 GPa

365   and 22 P–V points. Chang et al. (2015) suggested that the discrepancy in K_0' between their study and that

366   of Mao et al. (2011) was potentially due to the way density was estimated at high pressure by Mao et al.

367   (2011) by iteration, potentially leading to a higher K_0'.

368   We examined the effects of the selection of different crystal symmetry (monoclinic versus

369   orthorhombic) on the equations of state of wadsleyite by comparing XRD data evaluated using either

370   orthorhombic or monoclinic symmetry. In Figure 6, we compare P–V and F_E–f_E plots of the compression

371   data using orthorhombic symmetry versus using the observed monoclinic β-angles in calculating volume.

372   The results are compiled in Tables S3–S6, and S7. When fitting our P–V data to the BM3-EOS assuming

373   orthorhombic symmetry for the more hydrous wadsleyite (Z0570) we obtain: V_0 = 543.19(23) Å^3, K_{T0} =

374   164.0(2.7) GPa, and K_{T0}' = 4.26(23), whereas on using the monoclinic angles, we obtain: V_0 = 543.25(23)

375   Å^3, K_{T0} = 162.5(2.6) GPa, and K_{T0}' = 4.45(22). In short, these EOS parameters agree within their mutual

376   uncertainties, which is not surprising as the β-angle is not very distorted from 90° and the distortion only

377   showed a quite gradual increase with pressure above 10 GPa for sample Z0570. However, with the less

378   hydrous wadsleyite (Z0902), the BM3-EOS parameters assuming orthorhombic symmetry are: V_0 =

379   543.75(29) Å^3, K_{T0} = 165.7(3.4) GPa, and K_{T0}' = 5.51(28), whereas when using monoclinic symmetry and

380   the observed monoclinic β-angles, we obtain: V_0 = 543.09(22) Å^3, K_{T0} = 172.3(2.3) GPa, and K_{T0}' =

381   3.91(15). Assuming a fixed orthorhombic symmetry at all pressures produced lower K_{T0} values, but the

382   most pronounced effect is the higher first pressure derivative, K_{T0}'.

383

384   **Hydrogen bonds at high pressure**

385   The long O1–O4 edge of the M3 site is the primary location for hydrogen bonds in wadsleyite, as

386   previously determined by neutron diffraction (Purevjav et al. 2016). While the observed incompressibility

15

387   of the long O1–O4 edge in the very hydrous sample (Z0570) above 25 GPa might be interpreted as strong

388   hydrogen bonding, the fact that the long O1–O4 edge does not shorten below 2.90(1) Å, even up to the

389   highest pressure (Figure S5), indicates that the long O1–O4 hydrogen-bonded edge is still far longer than

390   what is considered strong hydrogen bonding, as defined by d(O…O) < 2.5–2.7 Å (Libowitzky 1999). In

391   contrast, high-pressure FTIR data (Yang et al. 2014) up to ~20 GPa and high-pressure Raman data up to

392   ~50 GPa (Kleppe et al. 2006) on hydrous wadsleyite show that the primary O–H stretching modes at

393   3360–3320 cm^{-1} (at 1 atm) gradually shift to lower frequency, reaching values below ~3200 cm^{-1} above

394   about 20 GPa, consistent with strong hydrogen bonding (Libowitzky 1999).

395   The primary hydrogen bond in wadsleyite, therefore, deviates significantly from the relation

396   between O...O distances and O–H stretching frequencies above 20 GPa (Figure 7). The simplest

397   explanation we can propose, though not prove, involves a shift of the hydrogen atom off the longer O1–

398   O4 edge of the M3 site either into the vacant M3 site or more along the c-axis above O1, either way

399   making the O1–H…O4 hydrogen bond angle even lower than the observed angle of 171° at room

400   pressure (Purevjav et al. 2016). If the hydrogen bond becomes more non-linear with pressure, the

401   hydrogen atom may move further away from the donor oxygen and O–H stretching frequency may

402   continue to drop, decoupling the O–H stretching frequency from the relation to hydrogen bond length for

403   linear hydrogen bonds (Libowitzky 1999). Future high-pressure polarized-FTIR measurements or high-

404   pressure neutron diffraction experiments of hydrous wadsleyite under hydrostatic compression might be

405   performed to test this hypothesis.

406

Implications

408   Wadsleyite is one of the most important minerals that control the physical and chemical

409   properties of the mantle transition zone. To better understand the effects of hydration on the physical

410   properties of wadsleyite at the atomic scale, single-crystal X-ray structure refinements of very hydrous

411   (2.0 wt% H_2O) and slightly hydrous (0.25 wt% H_2O) Fo$_{90}$ wadsleyite were used to evaluate the crystal

412   structure and hydrogen bond distances up to 32 GPa.

413　　　　At pressures exceeding 9 GPa, hydrous Fo_{90} wadsleyite deviates from orthorhombic symmetry to

414　　have monoclinic symmetry, which we interpret as resulting from the difference in compression behavior

415　　of the split M3 site due to Mg-Fe and vacancy ordering. An increase in the β-angle of hydrous wadsleyite

416　　with pressure has implications for equation of state parameters if lattice parameters are erroneously fitted

417　　to orthorhombic symmetry. When the monoclinic symmetry is used in high-pressure EOS fits, our results

418　　suggest that K_{T0} is lowered while K_{T0}' increases with hydration of wadsleyite. In wadsleyite,

419　　hydroxylation is associated with cation vacancies, and vacancies have been found to increase

420　　compressibility and K_{T0}' of other minerals such as spinels (Nestola et al. 2009). The demonstrated

421　　difference in calculated volume due to assumed orthorhombic symmetry, especially at $P > 10$ GPa where

422　　the monoclinic angle may increase, could partly explain some aspects of the controversial relationship

423　　between water content and K_0'. For example, the K_{T0}' values obtained by static compression for the same

424　　samples in this study (Z0570 and Z0902) and reported in Chang et al. (2015) assuming orthorhombic

425　　symmetry were identical and anomalously low with $K_{T0}' = 3.7(2)$, whereas we obtained $K_{T0}' = 4.5(2)$ for

426　　Z0570 and $K_{T0}' = 3.9(2)$ for Z0902. Therefore, our results show that ~2 wt% H_2O decreases the bulk

427　　modulus by about ~6% and increases K_{T0}' by about 17%. The decrease of K_{T0} and increase of K_{T0}' can

428　　cause a volume crossover on compression (Figure 2), although the more hydrous sample remains less

429　　dense at high pressure.

430　　　　The primary hydrogen bond in wadsleyite, defined by O1–H…O4 along the longer O1–O4 edge

431　　of the M3 site, becomes incompressible at pressures above 25 GPa. Although strong hydrogen bonding in

432　　wadsleyite above ~15 GPa is implied from previous spectroscopic studies showing O–H stretching

433　　frequencies that dropped below 3200 cm^{-1} (Yang et al. 2014; Kleppe et al. 2006), we found that the

434　　hydrogen bond distance, d(O1…O4), does not drop below 2.9 Å in length and certainly not into the

435　　region of strong hydrogen bonding at 2.5–2.7 Å. We conclude that the primary hydrogen bond in

436　　wadsleyite may become more non-linear at high pressures. This is the simplest explanation for the

437　　observed combination of a long O…O distance and low O–H stretching frequency and could be explained

438　　if the hydrogen atom moves off the long O1–O4 edge into the vacant M3 site or out above O1 more along

17

439   the c-axis. Due to isotopic effects on hydrogen-bond potential energy functions (e.g. k 1974), short, strong

440   hydrogen bonds are expected to be enriched in hydrogen versus deuterium (e.g. Kuroda et al. 1979). Even

441   though the hydrogen-bond length in wadsleyite determined here at transition zone pressures would not

442   predict strong isotopic fractionation (δD), the observed O–H stretching frequencies below 3300 cm^{-1}

443   (Yang et al. 2014) indicate otherwise, highlighting the importance of combining structure (XRD) and

444   spectroscopic evidence (e.g. Figure 7) to evaluate hydrogen-bonding geometry at pressures where neutron

445   diffraction is not yet feasible.

446

447

448   **Data Availability Statement**

449   All structure data as .cif files have been uploaded to the American Mineralogist Crystal Structure

450   Database.

451

452   **Acknowledgements**

18

464 Sergey Tkachev for help with gas loading, Joseph R. Smyth for synthesis of sample Z0902, and Jiyong

465 Zhao for assistance with the SMS data collection at Sector 3 of the APS.

466

467

468 **References**

469 Angel, R.J., Alvaro, M., & Gonzalez-Platas, J. (2014) Eosfit7c and a Fortran module (library) for

470   equation of state calculations. Zeitschrift für Kristallographie-Crystalline Materials, 229(5), 405-

471   419. https://doi.org/10.1515/zkri-2013-1711.

472 Buchen, J., Marquardt, H., Ballaran, T.B., Kawazoe, T., & McCammon, C. (2017) The equation of state

473   of wadsleyite solid solutions: Constraining the effects of anisotropy and crystal

474   chemistry. American Mineralogist, 102(12), 2494-2504. https://doi.org/10.2138/am-2017-6162.

475 Buchen, J., Marquardt, H., Speziale, S., Kawazoe, T., Ballaran, T.B., & Kurnosov, A. (2018) High-

476   pressure single-crystal elasticity of wadsleyite and the seismic signature of water in the shallow

477   transition zone. Earth and Planetary Science Letters, 498, 77-87.

478   https://doi.org/10.1016/j.epsl.2018.06.027.

479 Chang, Y.-Y., Jacobsen, S.D., Bina, C.R., Thomas, S.-M., Smyth, J.R., Frost, D.J., et al. (2015)

480   Comparative compressibility of hydrous wadsleyite and ringwoodite: Effect of H_2O and

481   implications for detecting water in the transition zone. Journal of Geophysical Research: Solid

482   Earth, 120(12), 8259-8280. https://doi.org/10.1002/2015JB012123.

483 Chopelas, A. (1991) Thermal properties of β-Mg_2SiO_4 at mantle pressures derived from vibrational

484   spectroscopy: Implications for the mantle at 400 km depth. Journal of Geophysical Research:

485   Solid Earth, 96(B7), 11817-11829. https://doi.org/10.1029/91JB00898.

486 Cynn, H., & Hofmeister, A.M. (1994) High pressure IR spectra of lattice modes and OH vibrations in Fe-

487   bearing wadsleyite. Journal of Geophysical Research: Solid Earth, 99(B9), 17717-17727.

488   https://doi.org/10.1029/94JB01661.

489 Deon, F., Koch-Muller, M., Rhede, D., Gottschalk, M., Wirth, R., & Thomas, S.-M. (2010) Location and

490   quantification of hydroxyl in wadsleyite: New insights. American Mineralogist, 95(2-3), 312-322.

491   https://doi.org/10.2138/am.2010.3267.

492 Dolomanov, O.V., Bourhis, L.J., Gildea, R.J., Howard, J.A., & Puschmann, H. (2009) Olex2: a complete

493   structure solution, refinement and analysis program. Journal of Applied Crystallography, 42(2),

494   339-341. https://doi.org/10.1107/S0021889808042726.

495 Dong, J.J., Fischer, R.A., Stixrude, L.P., & Lithgow-Bertelloni, C.R. (2021) Constraining the volume of

496   Earth's early oceans with a temperature-dependent mantle water storage capacity model. AGU

497   Advances, 2(1), e2020AV000323.

498 Emsley, J. (1980). Very strong hydrogen bonding. Chemical Society Reviews, 9(1), 91-124.

499 Fei, H., & Katsura, T. (2020) High water solubility of ringwoodite at mantle transition zone

500   temperature. Earth   and   Planetary   Science   Letters,   531,   115987.

501   https://doi.org/10.1016/j.epsl.2019.115987.

502 Gwanmesia, G.D., Whitaker, M.L., Dai, L., James, A., Chen, H., Triplett, R.S., & Cai, N. (2020) The

503   Elastic Properties of β-Mg_2SiO_4 Containing 0.73 wt.% of H_2O to 10 GPa and 600 K by Ultrasonic

504   Interferometry   with   Synchrotron   X-Radiation. Minerals, 10(3),   209.

505   https://doi.org/10.3390/min10030209.

506 Hazen, R.M. (1993) Comparative compressibilities of silicate spinels: anomalous behavior of (Mg,

507    $Fe)_2SiO_4$. Science, 259(5092), 206-209. https://doi 10.1126/science.259.5092.2.

508 Hazen, R.M., Weinberger, M.B., Yang, H., & Prewitt, C.T. (2000) Comparative high-pressure crystal

509   chemistry of wadsleyite, β-$(Mg_{1-x}Fe_x)_2SiO_4$, with x=0 and 0.25. American Mineralogist, 85(5-6),

510   770-777. https://doi.org/10.2138/am-2000-5-617.

511 Holl, C.M., Smyth, J.R., Jacobsen, S.D., & Frost, D.J. (2008) Effects of hydration on the structure and

512   compressibility   of   wadsleyite, β-Mg_2SiO_4.   American   Mineralogist, 93(4),   598-607.

513   https://doi.org/10.2138/am.2008.2620.

514   Horiuchi, H., & Sawamoto, H. (1981). β-Mg2SiO4: Single-crystal X-ray diffraction study. American

515   Mineralogist, 66(5-6), 568-575.

516   Jacobsen, S.D., Smyth, J.R., Swope, R.J., & Sheldon, R.I. (2000) Two proton positions in the very strong

517   hydrogen bond of serandite, NaMn$_2$ [Si$_3$O$_8$ (OH)]. American Mineralogist, 85(5-6), 745-752.

518   https://doi.org/10.2138/am-2000-5-613.

519   Jacobsen, S.D., Demouchy, S., Frost, D.J., Ballaran, T.B., & Kung, J. (2005) A systematic study of OH in

520   hydrous wadsleyite from polarized FTIR spectroscopy and single-crystal X-ray diffraction:

521   Oxygen sites for hydrogen storage in Earth's interior. American Mineralogist, 90(1), 61-70.

522   https://doi.org/10.2138/am.2005.1624.

523   Jacobsen, S.D., Holl, C.M., Adams, K.A., Fischer, R.A., Martin, E.S., Bina, C.R., et al. (2008)

524   Compression of single-crystal magnesium oxide to 118 GPa and a ruby pressure gauge for helium

525   pressure   media.   American   Mineralogist, 93(11-12),   1823-1828.

526   https://doi.org/10.2138/am.2008.2988.

527   Karato, S.I. (2011) Water distribution across the mantle transition zone and its implications for global

528   material   circulation. Earth   and   Planetary   Science   Letters,   301(3-4),   413-423.

529   https://doi.org/10.1016/j.epsl.2010.11.038.

530   Kleppe, A., Jephcoat, A., Olijnyk, H., Slesinger, A., Kohn, S., & Wood, B. (2001) Raman spectroscopic

531   study of hydrous wadsleyite (β-Mg$_2$SiO$_4$) to 50 GPa. Physics and Chemistry of Minerals, 28(4),

532   232-241. https://doi.org/10.1007/s002690100152.

533   Kleppe, A.K., Jephcoat, A.P., & Smyth, J.R. (2006) High-pressure Raman spectroscopic study of Fo$_{90}$

534   hydrous   wadsleyite.   Physics   and   Chemistry   of   Minerals,   32(10),   700-709.

535   https://doi.org/10.1007/s00269-005-0048-8.

536   Kohn, S., Brooker, R.A., Frost, D.J., Slesinger, A., & Wood, B. (2002) Ordering of hydroxyl defects in

537   hydrous   wadsleyite   (β-Mg$_2$SiO$_4$).   American   Mineralogist, 87(2-3),   293-301.

538   https://doi.org/10.2138/am-2002-2-310.

539   Kuroda, Y., Suzuoki, T., & Matsuo, S. (1979) The lowest δD value found in a hydrous silicate, pectolite.

540   Nature, 279, 227-228. https://doi.org/10.1038/279227a0.

541   Li, B., & Liebermann, R.C. (2000) Sound velocities of wadsleyite β-(Mg$_{0.88}$Fe$_{0.12}$)$_2$SiO$_4$ to 10

542   GPa. American Mineralogist, 85(2), 292-295. https://doi.org/10.2138/am-2000-2-305

543   Libowitzky, E. (1999) Correlation of OH stretching frequencies and OH…O hydrogen bond lengths in

544   minerals. Monatshefte   für   Chemie/Chemical   Monthly,   130(8),   1047-1059.

545   https://doi.org/10.1007/BF03354882.

546   Liu, W., Kung, J., Li, B., Nishiyama, N., & Wang, Y. (2009). Elasticity of (Mg$_{0.87}$Fe$_{0.13}$)$_2$SiO$_4$ wadsleyite

547   to 12 GPa and 1073 K. Physics of the Earth and Planetary Interiors, 174(1-4), 98-104.

548   https://doi.org/10.1016/j.pepi.2008.10.020.

549   Mao, Z., Jacobsen, S.D., Frost, D.J., McCammon, C.A., Hauri, E.H., & Duffy, T.S. (2011) Effect of

550   hydration on the single-crystal elasticity of Fe-bearing wadsleyite to 12 GPa. American

551   Mineralogist, 96(10), 1606-1612. https://doi.org/10.2138/am.2011.3807.

552   McMillan, P.F., Akaogi, M., Sato, R.K., Poe, B., & Foley, J. (1991) Hydroxyl groups in β-Mg$_2$SiO$_4$.

553   American Mineralogist, 76(3-4), 354-360.

554   Momma, K., & Izumi, F. (2011) VESTA 3 for three-dimensional visualization of crystal, volumetric and

555   morphology   data. Journal   of   applied   crystallography,   44(6),   1272-1276.

556   https://doi.org/10.1107/S0021889811038970.

557   Novak A. (1974) Hydrogen bonding in solids correlation of spectroscopic and crystallographic data.

558   InLarge Molecules (pp. 177-216). Springer, Berlin, Heidelberg.

559   Nestola, F., Smyth, J.R., Parisatto, M., Secco, L., Princivalle, F., Bruno, M., Prencipe, M., & Dal Negro,

560   A. (2009) Effects of non-stoichiometry on the spinel structure at high pressure: Implications for

561   Earth's   mantle   mineralogy. Geochimica   et   Cosmochimica   Acta, 73(2),   489-492.

562   https://doi:10.1016/j.gca.2008.11.001.

563   Pearson, D., Brenker, F., Nestola, F., McNeill, J., Nasdala, L., Hutchison, M., et al. (2014) Hydrous

564   mantle transition zone indicated by ringwoodite included within diamond. Nature 507(7491), 221.

22

565   https://doi.org/10.1038/nature13080.

566   Purevjav, N., Okuchi, T., Tomioka, N., Wang, X., & Hoffmann, C. (2016) Quantitative analysis of

567   hydrogen sites and occupancy in deep mantle hydrous wadsleyite using single crystal neutron

568   diffraction. Scientific Reports,6, 34988. https://doi.org/10.1038/srep34988.

569   Rivers, M., Prakapenka, V.B., Kubo, A., Pullins, C., Holl, C.M., & Jacobsen, S.D. (2008) The

570   COMPRES/GSECARS gas-loading system for diamond anvil cells at the Advanced Photon

571   Source. High Pressure Research, 28(3), 273-292. https://doi: 10.1080/08957950802333593.

572   Sano-Furukawa, A., Kuribayashi, T., Komatsu, K., Yagi, T., & Ohtani, E. (2011) Investigation of

573   hydrogen sites of wadsleyite: A neutron diffraction study. Physics of the Earth and Planetary

574   Interiors, 189(1-2), 56-62. https://doi.org/10.1016/j.pepi.2011.07.003.

575   Sheldrick, G.M. (2015) Crystal structure refinement with SHELXL. Acta Crystallographica Section C:

576   Structural Chemistry, 71(1), 3-8. https://doi.org/10.1107/S2053229614024218.

577   Smyth, J.R. (1987) β-Mg_2SiO_4; a potential host for water in the mantle? American Mineralogist, 72(11-

578   12), 1051-1055.

579   Smyth, J.R. (1994) A crystallographic model for hydrous wadsleyite (β-Mg2SiO4): an ocean in the

580   Earth's interior? American Mineralogist 79(9-10), 1021-1024.

581   Smyth, J.R., Kawamoto, T., Jacobsen, S.D., Swope, R.J., Hervig, R.L., & Holloway, J.R. (1997) Crystal

582   structure of monoclinic hydrous wadsleyite [β-$(Mg,Fe)_2SiO_4$]. American Mineralogist, 82(3-4),

583   270-275. https://doi.org/10.2138/am-1997-3-404.

584   Smyth, J.R., Bolfan-Casanova, N., Avignant, D., El-Ghozzi, M., & Hirner, S.M. (2014) Tetrahedral ferric

585   iron   in   oxidized   hydrous   wadsleyite. American   Mineralogist, 99(2-3),   458-466.

586   https://doi.org/10.2138/am.2014.4520.

587   Sturhahn, W. (2000) CONUSS and PHOENIX: Evaluation of nuclear resonant scattering data. Hyperfine

588   Interactions,125(1-4), 149-172. https://doi.org/10.1023/A:1012681503686.

589   Tsuchiya, J., & Tsuchiya, T. (2009). First principles investigation of the structural and elastic properties

590   of hydrous wadsleyite under pressure. Journal of Geophysical Research: Solid Earth, 114(B2).

591   https://doi.org/10.1029/2008JB005841.

592   Toellner, T.S., 2000. Monochromatization of synchrotron radiation for nuclear resonant scattering

593   experiments. Hyperfine Interactions. 125, 3-28. https://doi.org/10.1023/A:1012621317798

594   Wang, F., Barklage, M., Lou, X., van der Lee, S., Bina, C.R., & Jacobsen, S.D. (2018) HyMaTZ: A

595   Python program for modeling seismic velocities in hydrous regions of the mantle transition

596   zone. Geochemistry, Geophysics, Geosystems, 19(8), 2308-2324.

597   https://doi.org/10.1029/2018GC007464.

598   Yang, X., Keppler, H., Dubrovinsky, L., & Kurnosov, A. (2014) In-situ infrared spectra of hydroxyl in

599   wadsleyite and ringwoodite at high pressure and high temperature. American Mineralogist, 99(4),

600   724–729. https://doi.org/10.2138/am.2014.4634.

601   Ye, Y., Smyth, J.R., Hushur, A., Manghnani, M.H., Lonappan, D., Dera, P., & Frost, D.J. (2010) Crystal

602   structure of hydrous wadsleyite with 2.8% H_2O and compressibility to 60 GPa. American

603   Mineralogist, 95(1112), 1765-1772. https://doi.org/10.2138/am.2010.3533.

604   Ye, Y., Smyth, J.R., & Frost, D.J. (2011) Structural study of the coherent dehydration of

605   wadsleyite. American Mineralogist, 96(11-12), 1760-1767.

606   https://doi.org/10.2138/am.2011.3852.

607   Zhang, D., Dera, P.K., Eng, P.J., Stubbs, J.E., Zhang, J.S., Prakapenka, V.B., & Rivers, M.L. (2017) High

608   pressure single crystal diffraction at PXˆ2. JoVE (Journal of Visualized Experiments), e54660.

609   https://doi: 10.3791/54660.

610

611
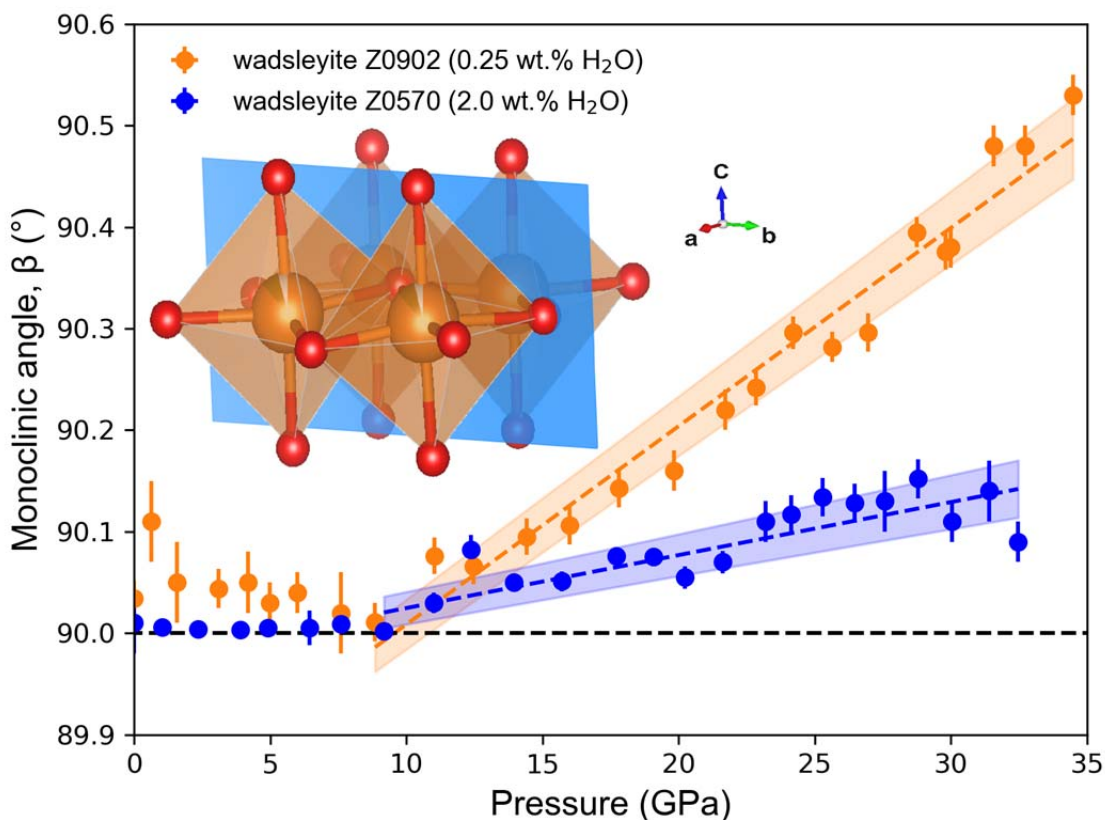
Figure 1. Monoclinic β-angle versus pressure of hydrous wadsleyite. Orange and blue dashed lines are linear fits to the data above 9 GPa for Z0902 and Z0570, respectively. The colored shaded regions indicate the 95% prediction bands. The black dashed line indicates the β-angle of the orthorhombic structure. The inset shows the local structure around the M3 octahedral site, wherein the blue plane indicates the mirror plane perpendicular to the *a*-axis for orthorhombic symmetry. The mirror plane is lost when vacancy ordering splits the M3 site into the non-equivalent M3A and M3B sites.

25

618
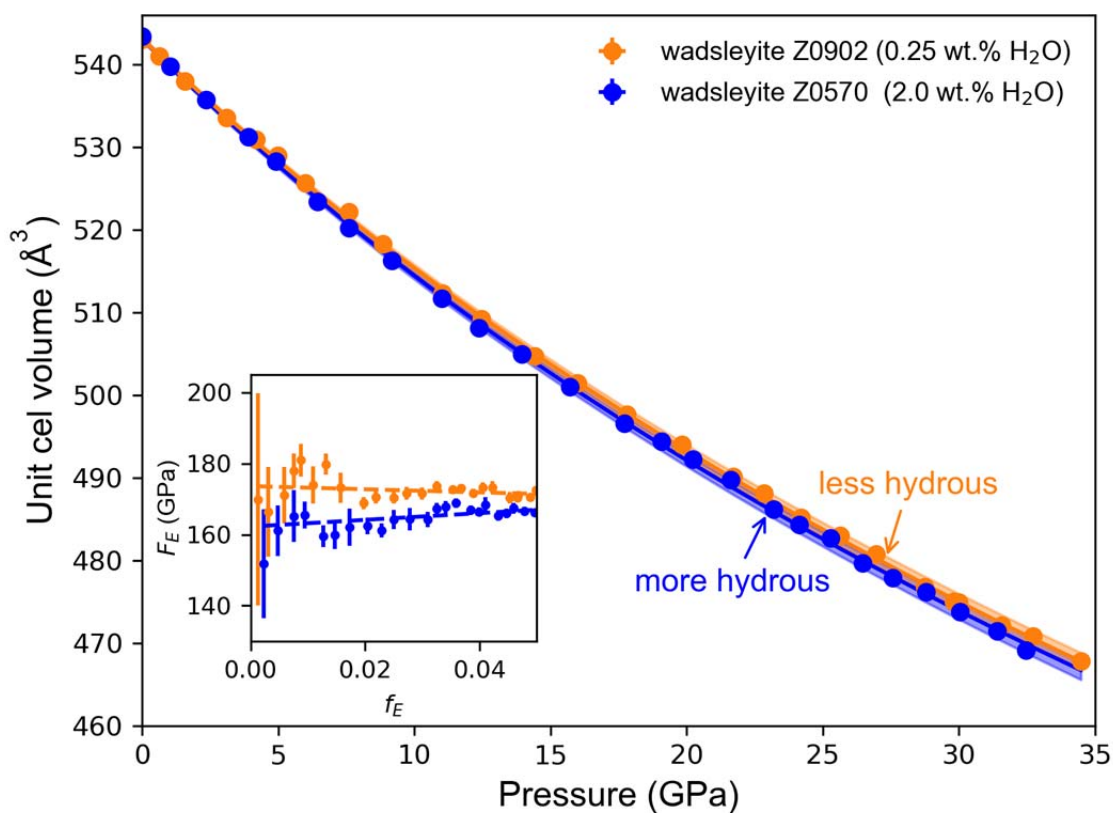
Figure 2. Unit cell volume *versus* pressure data for hydrous Fe-bearing wadsleyite. Fitted third-order

BM-EOS are shown as solid curves. The blue and orange shaded regions show the 95% prediction band.

The inset shows normalized pressure (F_E) versus Eulerian strain (f_E).

622

26

623
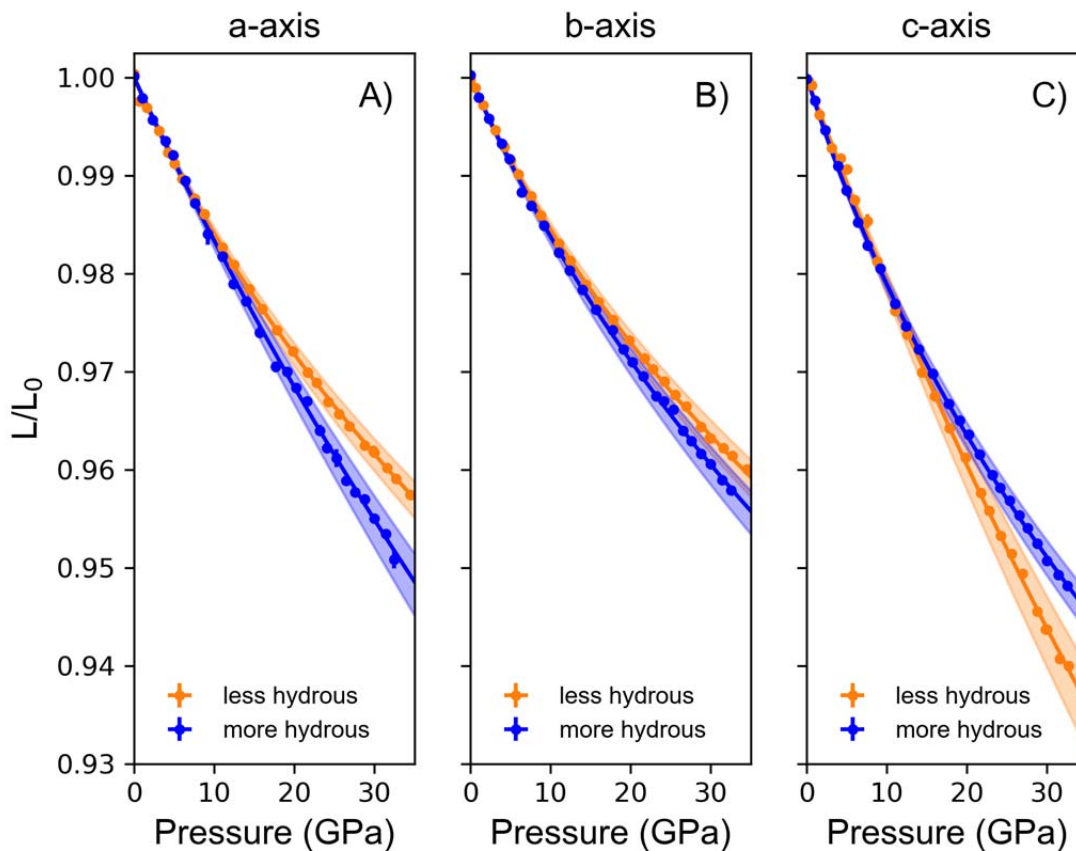
Figure 3. Axial compressibility of wadsleyite sample Z0570 with 2.0 wt% H_2O (blue data) and sample

Z0902 with 0.25 wt% H_2O (orange data). Fitted third-order BM-EOS fits are shown as solid curves. The

shaded regions show the 95% prediction band.

627
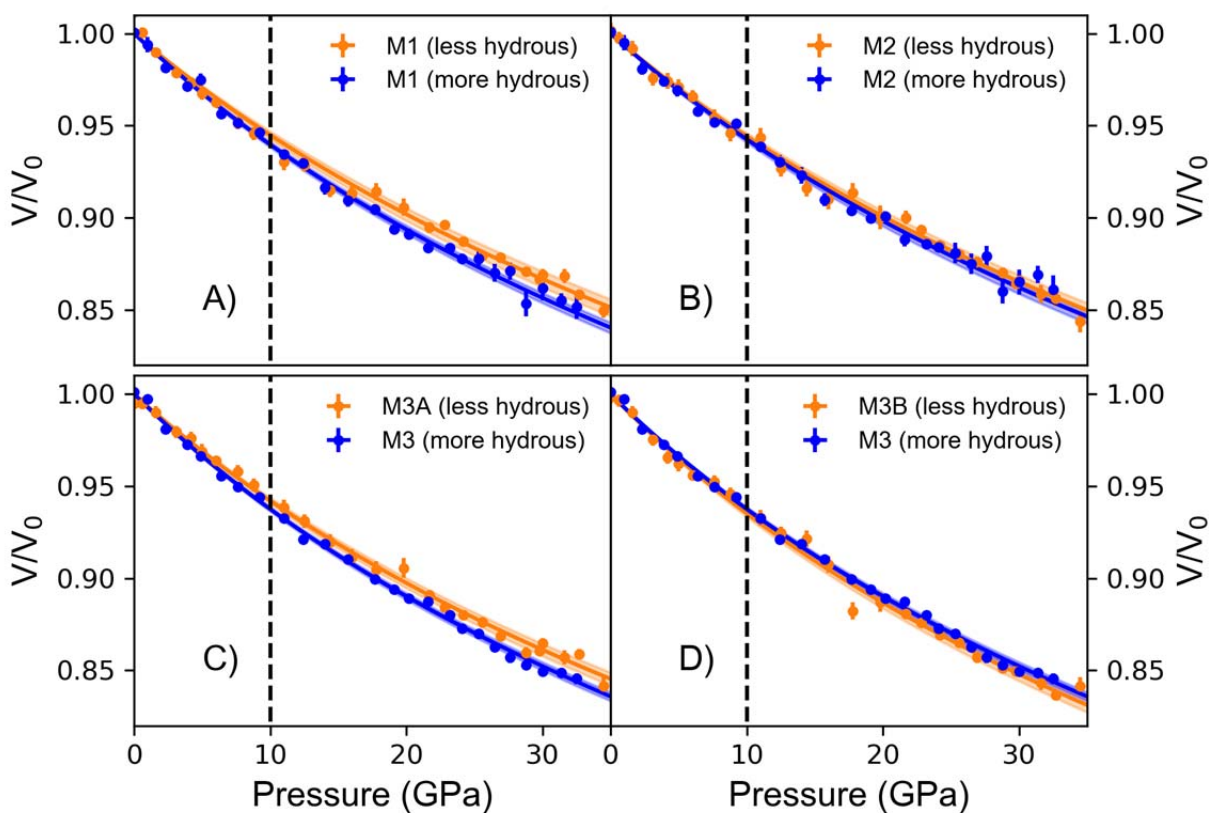
Figure 4. Octahedral volume compression of the A) M1, B) M2 and C) and D) M3 sites of hydrous wadsleyite sample Z0570 with 2.0 wt% H_2O (blue) and sample Z0902 with 0.25 wt% H_2O (orange). Solid lines show the fitted second-order BM-EOS. The shaded regions show the 95% prediction band. Dashed lines indicate the pressure at which the structure distorts from orthorhombic to monoclinic symmetry.

28

632
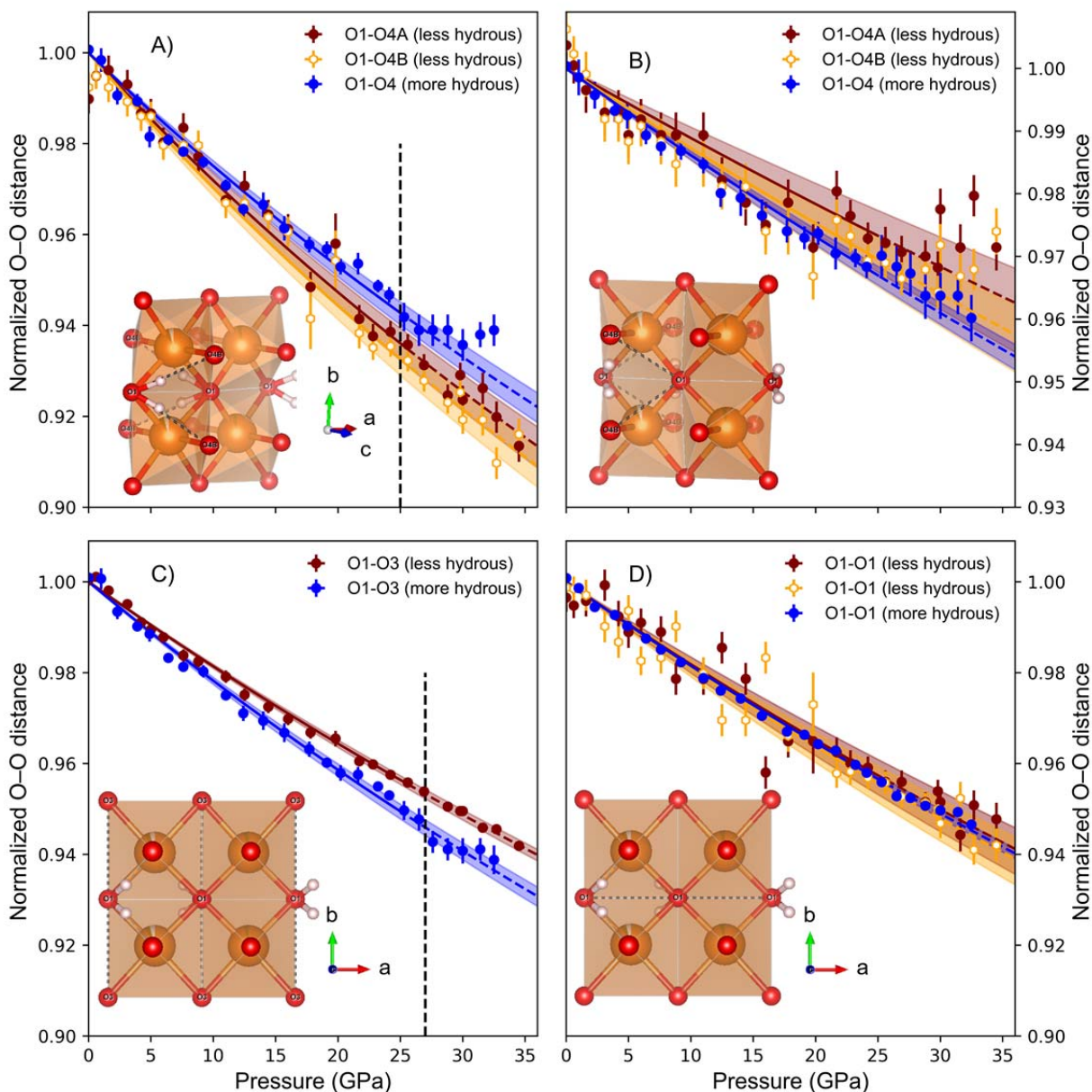
Figure 5. Compression of selected O…O interatomic distances in hydrous wadsleyite. A) The primary

hydrogen bond: in red and orange, long O1–O4 edges on the M3A and M3B sites for sample Z0902 with

0.25 wt% H_2O and monoclinic crystal symmetry. In blue, long O1–O4 edge on the M3 site in sample

Z0570 with 2.0 wt% H_2O and orthorhombic crystal symmetry. The dashed vertical line shows the

pressure above which the long O1–O4 edge of the M3 site stops shortening above ~25 GPa. B) Same as

panel A) but showing the short O1–O4 edges of the M3 sites. C) Other possible hydrogen bonds: O1–O3

639   of Z0902 and Z0570, with a dashed vertical line to show the pressure above which a possible change in

640   the O1–O3 compression occurs; D) O1–O1 of Z0902 and Z0570. The distances are normalized to the

641   distance at ambient pressure. Lines show the fitted second-order BM-EOS. Shaded regions show the 95%

642   prediction band. The insets show where the various O–O edges are located in the crystal structure.

643

644

645

646

647
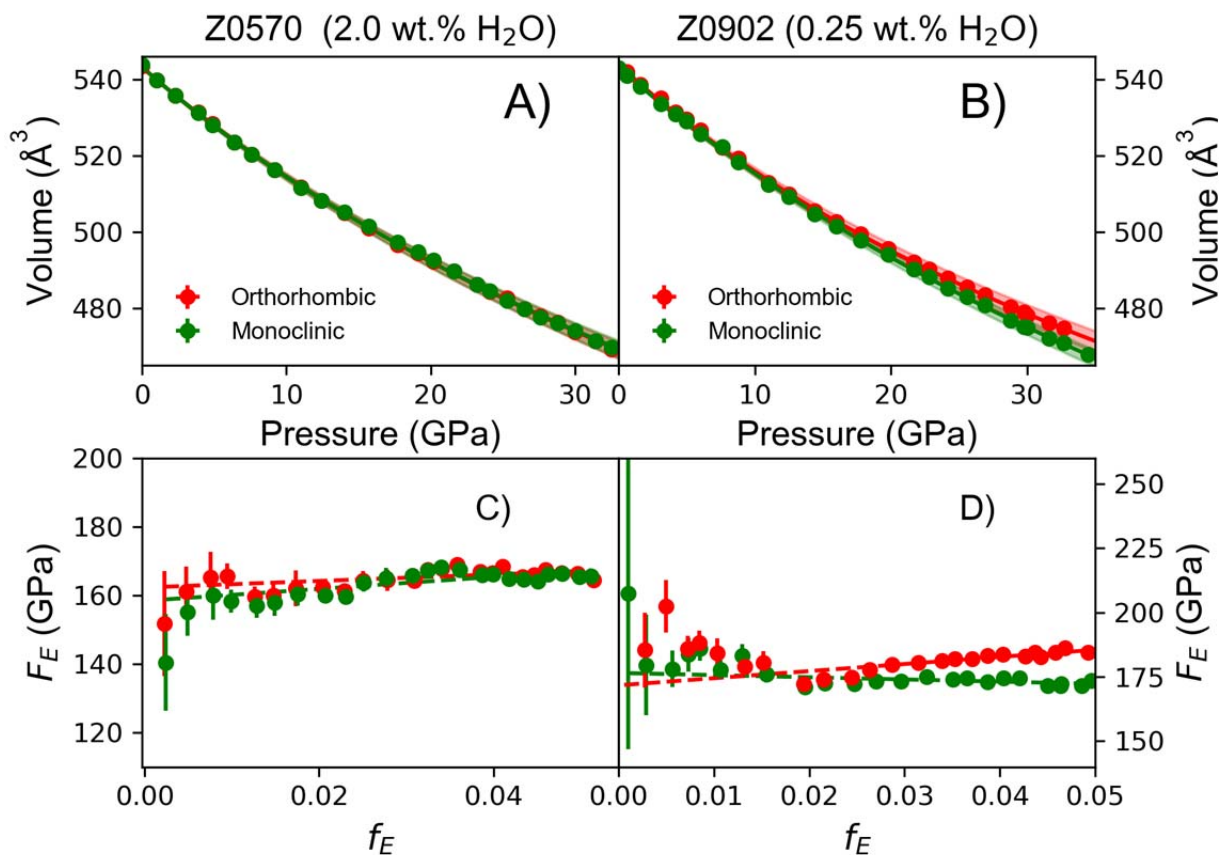
Figure 6. Unit cell volume versus pressure data of (A) more hydrous wadsleyite (Z0570, 2.0 wt% H_2O),

and (B) less hydrous wadsleyite (Z0902, 0.25 wt% H_2O) in both orthorhombic (red) and monoclinic

symmetries (green) with solid lines showing the fitted third⁻order BM-EOS. Panels (C) and (D) show the

corresponding normalized pressure (F_E) *versus* Eulerian strain (f_E), where the symmetry is either

orthorhombic (red) or monoclinic (green).

653
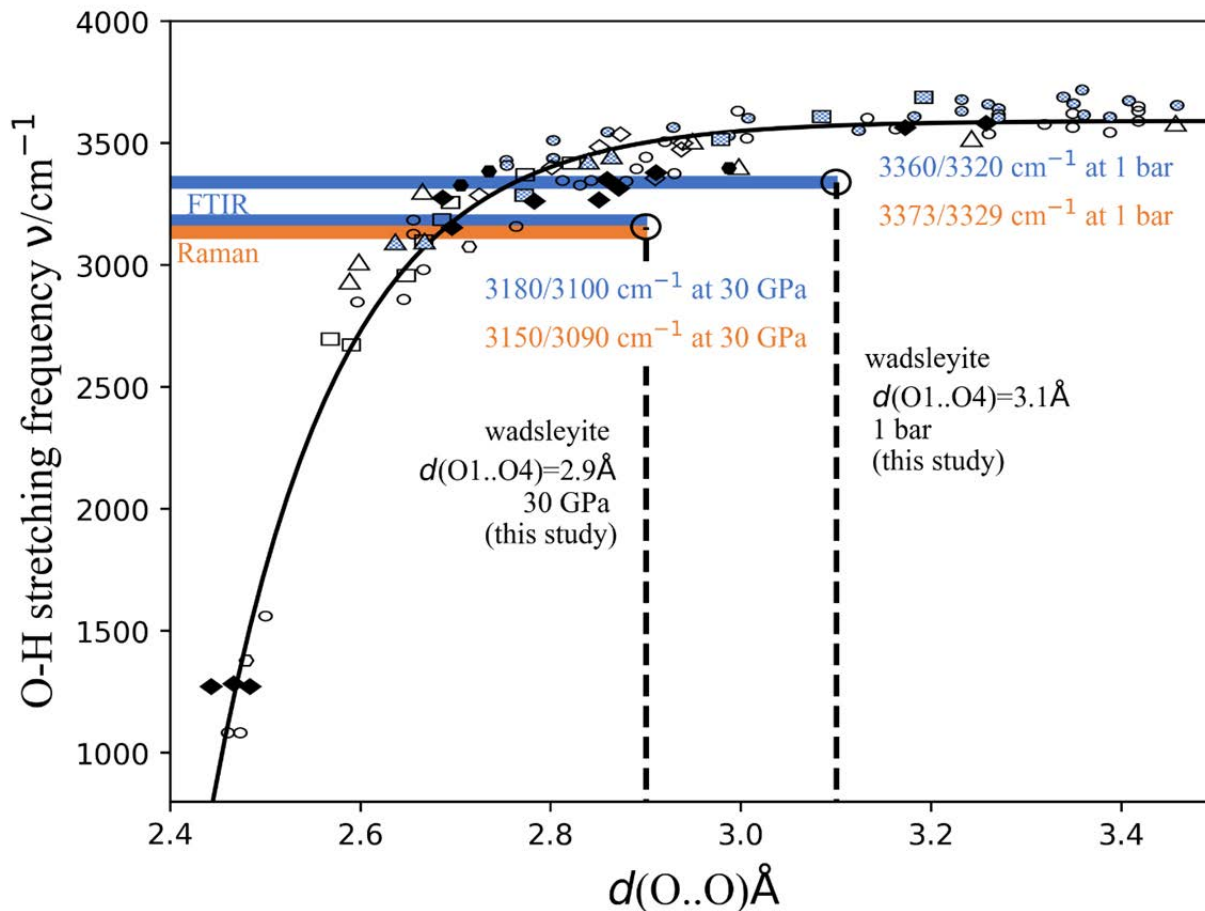
Figure 7. Compilation of hydrogen bond distances, d(O…O), *versus* O–H stretching frequencies for

nearly linear hydrogen bonds in minerals, modified from Libowitzky (1999). Large circles indicate the

intersection of measured d(O…O) for the O1–H…O4 hydrogen bond in wadsleyite from this study with

measured spectroscopic O–H stretching frequencies from FTIR (Yang et al. 2014) and Raman studies

(Kleppe et al. 2006). The FTIR O–H stretching frequencies of 3360 and 3320 cm^{-1} at 1 bar are from Yang

et al. (2014), and at 30 GPa (blue band) they are calculated from the polynomial fits published by Yang et

al. (2014) from data up to 20 GPa. The Raman O–H stretching frequencies at 30 GPa of 3090 and 3150

cm^{-1} are from the study of Kleppe et al. (2006).

662

663   **Table 1.** Comparison of hyperfine parameters of the two wadsleyite samples.

	Sample Z0570	Sample Z0902
$Fe^{3+}/\Sigma Fe$	24.7(1.1)%	12.8(1.0)%
Fe^{2+} isomer shift (mm/s)	1.04	1.04
Fe^{3+} isomer shift (mm/s)	0.082(9)	0.106(17)
Fe^{2+} quadrupole splitting (mm/s)	2.638(3)	2.657(4)
Fe^{3+} quadrupole splitting (mm/s)	0.358(9)	0.252(20)

664

665

666   **Table 2.** Compressibility of the coordination polyhedra of wadsleyite with 2.0 wt% H_2O (Z0570) and

667   with 0.25 wt% H_2O (Z0902).

Sample	M1 (GPa)	M2 (GPa)	M3 (GPa)	M3A (GPa)	M3B (GPa)	T (GPa)
Z0570	142(1.9)	150.7(2.4)	134.2(1.5)			314(10)
Z0902	154(3.5)	152.5(3.2)		145.9(3.2)	130.3(2.6)	316(13)

668

33